Effects of mirror seeing on high-contrast adaptive optics instruments

Melisa Tallis
Vanessa P. Bailey
Bruce Macintosh
Lisa A. Poyneer
Jean-Baptiste Ruffio
Thomas L. Hayward
Fredrik T. Rantakyrö
Jeffrey K. Chilcote
Dmitry Savransky
GPI Team

Effects of mirror seeing on high-contrast adaptive optics instruments

Melisa Tallis,[a,]* Vanessa P. Bailey,[a,b] Bruce Macintosh,[a] Lisa A. Poyneer,[c] Jean-Baptiste Ruffio,[a] Thomas L. Hayward,[d] Fredrik T. Rantakyrö,[d] Jeffrey K. Chilcote,[a,e] Dmitry Savransky,[f] and GPI Team

[a]Stanford University, Kavli Institute for Particle Astrophysics and Cosmology, Physics Department, Stanford, California, United States
[b]Jet Propulsion Laboratory, California Institute of Technology, Pasadena, California, United States
[c]Lawrence Livermore National Laboratory, Livermore, California, United States
[d]Gemini Observatory, La Serena, Chile
[e]University of Notre Dame, Department of Physics, Notre Dame, Indiana, United States
[f]Cornell University, Sibley School of Mechanical and Aerospace Engineering, Ithaca, New York, United States

Abstract. Ground-based direct imaging surveys such as the Gemini Planet Imager Exoplanet Survey (GPIES) rely on adaptive optics (AO) systems to image and characterize exoplanets that are up to a million times fainter than their host stars. One factor that can reduce AO performance is turbulence induced by temperature differences in the instrument's immediate surroundings (e.g., "dome seeing" or "mirror seeing"). In this analysis, we use science observations, AO telemetry, and environmental data from September 2014 to February 2017 of the GPIES campaign to quantify the effects of mirror seeing on the performance of the Gemini Planet Imager (GPI) instrument. We show that GPI performance is optimal when the primary mirror (M1) is in equilibrium with the outside air temperature. We then examine the characteristics of mirror seeing by calculating the power spectral densities (PSDs) of spatial and temporal Fourier modes. Inside the inertial range of the PSDs, we find that the spatial PSD amplitude increases when M1 is out of equilibrium and that the integrated turbulence may exhibit deviations from Kolmogorov atmospheric turbulence models and from the one-layer frozen flow model. We conclude with an assessment of the current temperature control and ventilation strategy at Gemini South. © *2020 Society of Photo-Optical Instrumentation Engineers (SPIE)* [DOI: 10.1117/1.JATIS.6.1.015002]

1 Introduction

Direct imaging is a technique used for the detection and characterization of gas giant exoplanets and their formation environments. Each newly imaged planet helps constrain planet populations and provides a laboratory to study the formation, evolution, and atmospheric chemistry of massive, young, self-luminous planets, which are also referred to as "young Jupiters."[1–7] Known young Jupiters are $\sim 10^4$ to 10^7 times fainter than their host stars in the near-infrared and are often separated by less than 0.5 arc sec. Specifically designed high-contrast instrumentation on large ground-based telescopes can spatially resolve these faint sources from their host stars. The Gemini Planet Imager (GPI) on the 8-m telescope at the Gemini South (GS) Observatory is one such instrument; it employs adaptive optics (AO) to correct for atmospheric turbulence and a coronagraph for starlight suppression.[3,8–10]

---

*Address all correspondence to Melisa Tallis, E-mail: mtallis@stanford.edu

To improve the sensitivity of current and future high-contrast instruments, it is critical to understand the factors limiting the performance of current high-contrast systems. Turbulence uncorrected by the AO system has been identified as a major limiting factor for performance.[10–12] The residual turbulence produces speckles in the point spread function (PSF), which reduce the instrument's sensitivity.[13,14] Speckle behavior depends on the turbulence source. The effects of the high-altitude jet stream and dome turbulence have been studied extensively.[15–17] This work explores the contribution from a different source: mirror seeing.

Turbulence can be parameterized in several ways. The amount of power in phase variations in each spatial or temporal Fourier mode, called the power spectral density (PSD), is one metric. The PSD of atmospheric turbulence is generally assumed to follow the Von Karman spectrum;[18] for simplicity, we assume a scale-free Kolmogorov spectrum:[19–22]

$$\text{PSD} = 10^\alpha f^\beta, \tag{1}$$

where f is Fourier mode, 10^α is the amplitude of the PSD, and β is the power-law index of the PSD. We use the following convention to distinguish between spatial and temporal PSD parameters: spatial PSD parameters are denoted with a subscript "s," and temporal PSD parameters are denoted with a subscript "t." The rate at which energy is transferred from large-scale eddies to small-scale eddies is embodied in β. In frozen flow turbulence,[23] $\beta_s = -11/3$ and $\beta_t = -8/3$.[24] This assumption implies that a single layer of turbulence can be regarded as a fixed phase screen propagating horizontally through the atmosphere. The strength and speed of the turbulence are frequently distilled into two parameters: the coherence length and the coherence time denoted as r_0 and τ_0, respectively. The coherence length, also called the Fried parameter, describes the lateral distance across the aperture in which the RMS phase aberration of the incoming wavefront is one radian. The full width at half maximum (FWHM) of the PSF, also called the seeing disk, is $\epsilon_0 \sim \lambda/r_0$, where λ is the observing wavelength. The coherence time, $\tau_0 \propto r_0/v_0$, where v_0 is the characteristic velocity of the turbulence. AO systems are generally designed using these turbulence models with assumptions about the local r_0 and τ_0 values of the observatory.[15] If any of these assumptions are violated, there is a risk of underdesigning the system in some aspect, whether it is deformable mirror (DM) stroke budget or loop speed.

Turbulence introduced in and around the telescope dome can lead to mediocre performance on nights with otherwise exceptional observing conditions. We use the general term "dome seeing" to refer to any source of additional turbulence in the dome and "mirror seeing" to refer to turbulence sourced specifically from the telescope mirror(s). Studies done with seeing-limited instruments found that the PSF FWHM and Strehl ratio (the ratio of the peak PSF intensity to that of a perfect Airy pattern) are strongly correlated with temperature differences throughout the dome.[25,26] Furthermore, laboratory studies observed that mirror seeing develops as soon as the mirror's temperature exceeds the ambient air temperature.[27] Recent results from Robo-AO are also suggestive of the effects of dome seeing on AO instrumentation.[28] Anecdotally, some GPI datasets have shown poorer performance on nights with otherwise exceptional seeing conditions, as measured by the observatory seeing monitors. This motivates the need for a study of mirror seeing that pertains to high-contrast imaging. Although, we limited our study to a single instrument, these results could also be generalized to other Gemini instruments, such as GEMS or ALTAIR, and likely to other observatories as well.

According to the above studies, the key to reducing dome seeing is to control the temperature inside the dome. For the past few years, the temperature control strategy at GS has been to measure the outside air temperature near the start of each night, and then use that temperature as the set point for the dome air conditioning for the following afternoon. This strategy performs well when the weather is stable, but it is not ideal when weather fronts cause rapid changes in temperature from one day to the next. The primary mirror (M1) temperature is not actively controlled and is often considerably warmer than the outside air as it is a large, heavy structure with a much slower cool-down rate.

In this work, we investigate the effects of mirror seeing on AO performance, using data from the Gemini Planet Imager Exoplanet Survey (GPIES).[29] GPIES is a direct imaging campaign that began in 2014 to search for exoplanets and circumstellar disks around ~600 young, nearby stars. Each campaign observation is archived together with observatory environmental metadata and

AO telemetry. This large, uniform dataset enables us to study the relationship between various environment and telescope parameters with GPI performance. Additionally, we can do a more detailed analysis of mirror turbulence with the AO telemetry data. The datasets used in this study are described in Sec. 2. The filtering and matching of datasets as well as the techniques used to calculate turbulence parameters are described in Sec. 3. Our results are presented and discussed in Sec. 4. We conclude in Sec. 5.

2 Data

2.1 *GPIES Observations*

A GPIES campaign observation is comprised of 20 to 40 sequential H-band (1.6 μm) integral field spectrograph (IFS) images, each with a 60-s exposure. Each exposure is automatically reconstructed into a spectral cube (x, y, and λ), which we refer to as "raw images." A record of the instrument, observatory, and ambient environment states, along with a time stamp and target identification information, are saved in the image header. At the end of an observing sequence, individual raw IFS images automatically undergo calibration and PSF-subtraction and are combined into a single "final" IFS image by the GPIES data pipeline.[30–33]

An important metric used for monitoring GPI's performance is contrast, the minimum detectable planet-to-star flux ratio at a given projected separation from the host star. The 5σ contrast at a given separation is defined as five times the local standard deviation of the noise in an annulus centered at that separation. This calculation first takes place for each wavelength slice in a cube, and then the values for the central 50% of the spectral band are median-combined to produce a single contrast curve that is associated with the observation.[31,33] Typical "raw contrast" values at 0.4 arc sec are $\lesssim 10^{-4}$. The "final contrast" is typically 10 to 50 times better than the raw contrast.

The raw and final data products are logged in the GPIES database as they are produced.[34] This includes the raw and final 5σ contrast measured at 0.2 arc sec, 0.4 arc sec, and 0.8 arc sec separations. For simplicity, we consider only the raw and final contrast at 0.4 arc sec separation. At smaller separations, performance can be affected by coronagraph misalignment, and at larger separations, images may be background limited.[11] In total, we have access to 28,387 raw images and 719 final images, which were gathered between November 2014 and January 2019.

2.2 *GPI AO Telemetry*

GPI's AO system[10] consists of a Shack–Hartmann wavefront sensor (WFS) and two DMs. The WFS uses 2×2 pixel quad-cell centroiding to measure the slope of the wavefront across each subaperture in the full telescope aperture, which is 43 subapertures wide. Each subaperture samples 18 cm of the wavefront, and these measurements are performed at a rate of 1 kHz on stars brighter than eighth magnitude in I-band and 500 Hz on fainter stars. The phase of the wavefront is reconstructed in Fourier modes.[35] Low-order modes are sent to the woofer DM and the tip/tilt stage; high-order modes are sent to the tweeter DM. The real-time control computer estimates the modal coefficients for tip, tilt, and focus and removes them from the signal that drives the control loop.

Several types of AO data are periodically recorded for analysis purposes, 2 to 5 times per target, at the discretion of the observer. A full telemetry set contains a record of the WFS measurements, DM, and tip/tilt commands, along with any other offsets applied. The datasets used here are 10- to 22-s long, and a total number of 2009 AO telemetry sets were recorded between September 2014 and January 2019.

A direct measurement of the AO system's performance is the residual wavefront error (σ_{WFE}), defined as the error measured by the WFS after applying a correction with the DM. An instantaneous approximation of σ_{WFE}, based on the RMS subaperture slopes, is saved to the header of each raw IFS frame (see Sec. 3.1). We also estimated the σ_{WFE} from reconstructed wavefront telemetry as discussed in Sec. 3.2.

2.3 Gemini Observatory Data

There are multiple temperature sensors placed in and around the telescope dome at GS. Each sensor records the temperature every 5 min. The approximate locations of the interior sensors relevant to this study are displayed in Fig. 1. At each location, there is one sensor directly attached to the metal truss surface (Minco S651PDX24B[36]) and another that is suspended freely in the air next to it (Omega RDT-805[37]). On M1, there are two individual sensors mounted directly on the outer rim. The "M1-Y" sensor is attached to the side that tips downward when the telescope slews to a lower elevation, while the "M1+Y" sensor is attached to the side that tips upward. The precision of the temperature data is ~1% at 25°C, according to the sensor specifications. Although precise, the sensors may be subject to constant bias offsets, as will be discussed in Sec. 3.1. Additionally, the outside air temperature is recorded by a weather tower adjacent to GS.

The ϵ_0 and τ_0 values at the time of observation were provided by the observatory's Differential Image Motion Monitor (DIMM) and Multi-Aperture Scintillation Sensor (MASS), respectively.[38] These instruments are not located in the dome, but rather in a separate tower ~80 m away. Consequently, they are insensitive to mirror or dome seeing, a crucial point for our study.

3 Methods

3.1 Filtering, Matching, and Calibrating GPI Science Data and Temperature Readings

IFS raw and final datasets were filtered as follows. To ensure high signal-to-noise images and telemetry, we included in our sample only bright stars (I-band magnitude <7). This also guaranteed that the AO system was operating at 1 kHz for all images in the sample. We also excluded images that were taken in the worst seeing conditions or when there was no recent measurement (≲40 min) from the MASS/DIMM. According to the MASS/DIMM, the median seeing recorded at Cerro Pachon from the years 2014 to 2019 was $\epsilon_0 = 0.9$ arc sec and $\tau_0 = 1.5$ ms. We only kept the images corresponding to the best 85% seeing conditions: $\epsilon_0 < 1.2$ arc sec and $\tau_0 > 0.8$ ms. These seeing cuts combined culled almost 80% of the remaining dataset, in large part because no MASS/DIMM values were available after early 2017. Next, we rejected final images in which the field of view (FOV) rotated by less than twice the FWHM of the PSF for a planet orbiting its star at 0.4 arc sec($\theta_{\text{FOV}} > 12.2$ deg) ($\theta_{\text{FOV}} > \frac{2\lambda}{D\rho}$, where $\lambda = 1.65$ μm, $D = 8$ m, and $\rho = 0.4$ arc sec). The final contrast depends on the FOV rotation because the
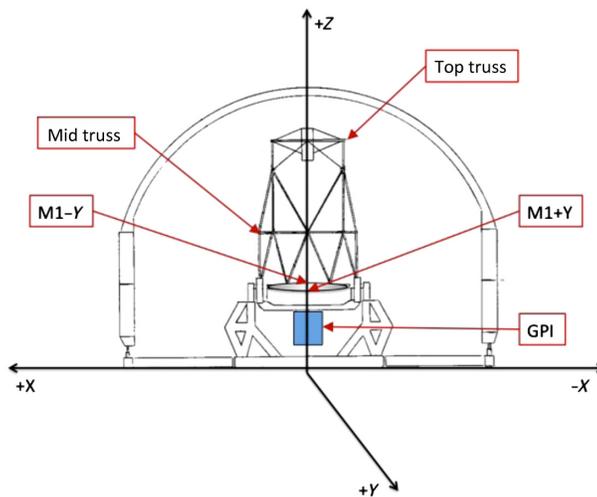

Fig. 1 Schematic of GS telescope and observatory dome. Arrows mark the locations of temperature sensors.

GPI data pipeline relies in part on the angular differential imaging observing technique. Sequences with a lower FOV rotation suffer loss of sensitivity due to self-subtraction during the PSF subtraction process. After all of these cuts, 2977 raw frames and 120 final images remained. The remaining data represent 57 different observing nights between September 2014 and February 2017.

Finally, not all sequences attained the same total integration time. To normalize all values to an equivalent of a full sequence (38 min), we scaled final contrast by $\sqrt{t_i/38 \text{ min}}$, where t_i is the total integration time. This scaling was verified to hold after the minimum θ_{FOV} was achieved, based on a multihour c Eri dataset.

The approximate σ_{WFE} that is stored in the IFS headers is overestimated because the calibration between the RMS displacement of the WFS centroids and the actual wavefront error was never measured. We obtained the linear relationship:

$$\sigma_{\text{AO telemetry}} = (81.01 \pm 0.02)10^{-2}\sigma_{\text{IFS header}} - (20 \pm 4)(\text{nm RMS}), \tag{2}$$

using a subset of images that had contemporaneous residual phase maps reconstructed from full AO telemetry (as described in Sec. 3.2). The data and fit are displayed in Fig. 2. We corrected all IFS header values using this fit.

We also filtered and calibrated the GS temperature data. Bad or missing data in the GS temperature logs are recorded with a null value; these entries were removed. We cross-checked the M1 temperatures against simultaneous readings from the GPI AO bench temperature sensor and the dome air and truss sensors. Both M1 sensors revealed significant offsets. The observatory staff calibrated these two sensors on August 3, 2017. Unfortunately, the offsets were not recorded during the calibration process. To correct the historical data, we determined the zero-point offset for each sensor in the following way: first, we split the data into before and after calibration sets—from January 1, 2014, to August 2, 2017, and from August 4, 2017, to December 31, 2018—and then folded them by year. Next, we fit a line to the before calibration data from August 4 to December 31 and subtracted the fit from the after calibration data. In the final step, we calculated the DC offset that made the mean of the difference equal to zero. The average offset value for each sensor is displayed in Table 1. The dome air temperature reported by the various truss air temperature sensors also showed moderate systematic offsets. The lower-truss sensor reading most closely matched the temperature reported by the weather tower, while the upper- and mid-truss sensors reported temperatures 1°C to 2°C cooler. Because the calibration of these sensors was not independently checked as M1 sensors were, we chose to use only the readings from the lower-truss sensor. However, we stress that absolute temperatures were not essential in this study as we investigated only the relationship between GPI performance and relative temperature changes.
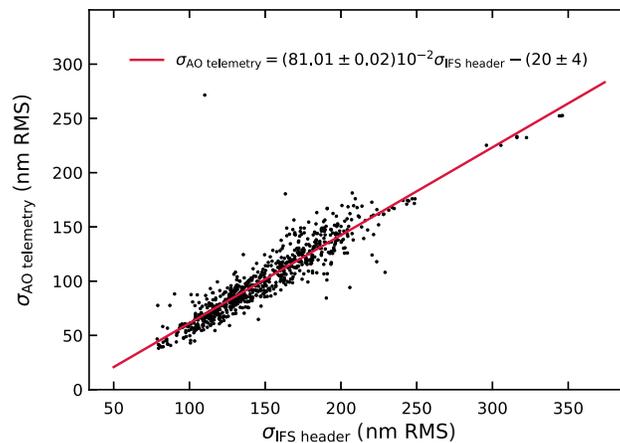

Fig. 2 Comparison of residual wavefront error derived from AO telemetry, $\sigma_{\text{AO telemetry}}$, to the instantaneous approximation saved to the IFS image headers, $\sigma_{\text{IFS header}}$ (black points). The linear fit is overlaid (red line) and was used to correct $\sigma_{\text{IFS header}}$ in subsequent analysis.

Table 1 Calculated temperature offsets for GS temperature sensors ($T_{\text{corrected}} = T_0 + \text{offset}$).

Sensor	Offset (°C)
M1+Y	3.5
M1-Y	2.1

Ultimately, a single value of each environment parameter (M1 temperature, dome temperature, τ_0, and ϵ_0) was associated with each raw and final image for all subsequent analysis. We averaged the two corrected M1 sensors to produce an instantaneous M1 temperature. We matched each raw science frame with its closest-in-time temperature readings. If no temperature was recorded within 30 min of the observation, we excluded the image from our sample; this removed ~25 of the raw images. Finally, we matched final science frames with the average M1 and dome temperatures and the average seeing recorded during the entire observation sequence.

3.2 Characterizing Turbulence with AO Telemetry

We quantified the characteristics of mirror turbulence by examining the spatial and temporal PSDs of the wavefronts at the entrance pupil (i.e., before AO correction). In theory, it is possible to directly measure mirror seeing with open-loop measurements from the WFS. But in practice, open-loop wavefront errors are too large to be measured by GPI's WFS. Thus, rather than directly measuring the open-loop phase, we reconstructed the "pseudo open-loop" phase from closed-loop AO telemetry. A detailed description of this process can be found in Refs. 39 and 40. The closed-loop residual phase measured by the WFS, Φ_{WFS}, is given by

$$\Phi_{\text{WFS}} = \Phi_A - \Phi_{\text{DM}}, \tag{3}$$

where Φ_A is the pseudo open-loop phase and Φ_{DM} is the DM commanded phase. Each pseudo open-loop time series was mapped onto a slightly oversized cube containing (48×48) subapertures $\times 22,000$ ms, with a pixel scale of 0.18 m at M1. Any uncontrolled data points, such as those located outside the aperture area, on the aperture edge, or behind the secondary mirror, were set to zero.

Tip and tilt were already removed from the signal by the real-time control computer; however, some static aberrations remained. To estimate the low-order static aberrations, we calculated the time-average phase map and fit it with the first six Zernike polynomials, under the assumption that any low-order turbulence-induced wavefront error would average to zero over the 10- to 22-s time series. We used the Python optical simulation package Poppy[41] to calculate normalized Zernike coefficients.

We then used the two-dimensional discrete Fourier transform (DFT) to decompose the phase signal at each timestep into its Fourier modes. Given the open-loop phase $\phi(x, y, t_i)$ and the aperture $a(x, y)$, the modal coefficients at each time step t_i are

$$F_{xy}(k_x, k_y, t_i) = \frac{1}{\sum_{x=0}^{N-1} \sum_{y=0}^{N-1} a(x, y)} \sum_{x=0}^{N-1} \sum_{y=0}^{N-1} \phi(x, y, t_i) a(x, y) e^{-2\pi j(k_x x + k_y y)}. \tag{4}$$

Computing the square of the spatial modes yields the spatial PSD, which is as follows:

$$P_{xy}(k_x, k_y) = \langle |F_{xy}(k_x, k_y, t)|^2 \rangle_t, \tag{5}$$

where $\langle \rangle_t$ is the time-average of the individual PSDs. An example of the spatial PSD (left) and the temporal PSD (right) of the turbulence recorded while observing c Eri on December 19, 2015, is shown in Fig. 3.
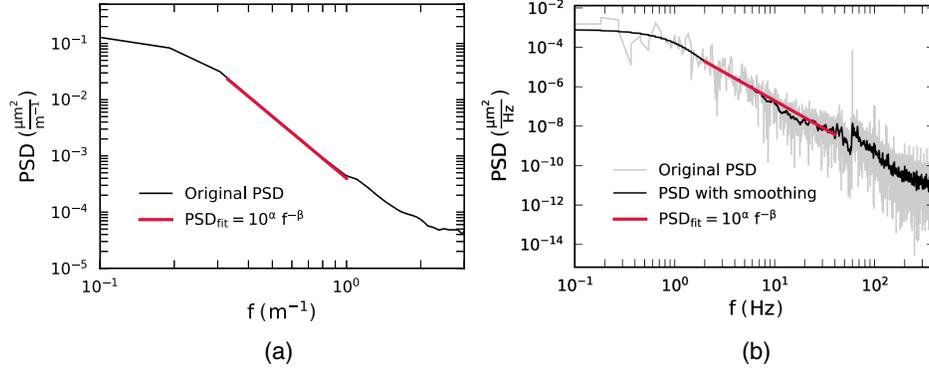
Fig. 3 (a) Spatial and (b) temporal PSDs of pseudo open-loop wavefront errors derived from AO telemetry recorded while observing c Eri on December 19, 2015. We superimposed the temporal PSD obtained after applying the Savitzky–Golay filter (black) with the original temporal PSD (gray). Power law fits (red line) were performed in the inertial range of the PSDs.

The length scales captured by GPI range from 0.36 to 8 m, where 0.36 m is twice one sub-aperture diameter and 8 m is the full aperture diameter. We fit a power law of the form PSD $= 10^{\alpha_s} f^{\beta_s}$ from the middle region of the spectrum $(0.3\ \text{m}^{-1}, 1.0\ \text{m}^{-1})$, which is highlighted in Fig. 3. This selection ensures that our parameters are free from tilt and outer scale effects at lower spatial frequencies and WFS aliasing effects at higher spatial frequencies.

This process was repeated to estimate the average temporal PSD of the DM actuators:

$$P_t(\omega) = \langle |F_t(x, y, t)|^2 \rangle_{xy}, \tag{6}$$

where $\langle \rangle_{xy}$ is the average of all the DM actuators in the aperture and the DFT of each time series is equal to

$$F_t(\omega) = \frac{1}{N} \sum_{t=0}^{N-1} \phi(x, y, t) a(x, y) e^{-2\pi j(\omega t)}. \tag{7}$$

The resulting temporal PSD, which is displayed in Fig. 3 on the right, appears noisier than the spatial PSD because the position of each DM actuator is more finely sampled than the spatial modes. Thus, we used a Savitzky–Golay[42] filter with a window length of 101 ms and polynomial order of 5 to reduce the noise in the temporal PSD. The Savitzky–Golay filter splits the data into discrete segments and approximates the data inside each interval with a polynomial fit. After we smoothed the PSD, we fit a power law of the form PSD $= 10^{\alpha_t} f^{\beta_t}$ from (2 and 40 Hz) to avoid potential biases associated with aliasing and/or vibrations that may be introduced by the telescope.

4 Results

4.1 *Temperature Conditions at Gemini South*

We first investigated the typical temperature conditions at GS using temperature records from the years 2015 to 2019, which include all nights, not only those with GPI data. We excluded nights with only partial records. We required at least 10 measurements recorded in a 24-h period and at least 4 h between $T_{\max}$ and $T_{\min}$. A total of 1001 nights, out of an original 1221, remained. Figure 4(a) shows a histogram of $(T_{\max} - T_{\min})$ of the outside air for each calendar day, split at sunset. The distribution peaks at 4°C but occasionally reaches 15°C, illustrating the wide range of day–night temperature swings that the observatory must cope with. We measured the night-time instantaneous temperature differences between M1, dome air, and ambient air to identify potential sources of dome seeing. We only considered nights in which GPI took on-sky data. We plot their density histograms in Fig. 4(b) and their cumulative densities in Fig. 4(c). The reported
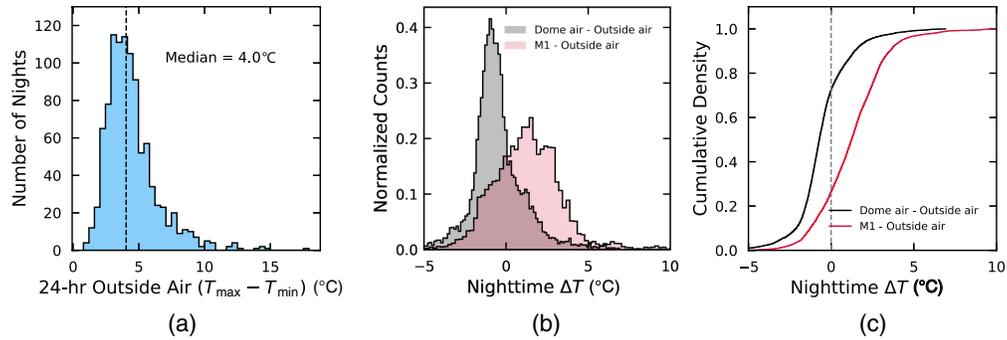
Fig. 4 Temperatures at the GS Observatory. (a) Histogram of the daily min–max range of outside air temperatures. (b) Histogram of instantaneous temperature differences between dome air or M1 and outside air at night, for those nights when GPI was observing, with DC offset corrections as described in Sec. 3.1. (c) Cumulative density plot of the data in (b).

median temperature of the dome is 0.7°C cooler than ambient, while the reported median temperature of M1 is 1.2°C warmer than ambient. However, as discussed previously, while the calibration of the M1 sensors has been validated, those of the outside air sensor and the dome air sensor have not. Thus, while the distributions of dome–ambient and M1–ambient difference are correct, the medians could be biased. From the standard deviations of the two distributions (1.6° C and 2.0°C, respectively), we can conclude that the dome more quickly tracks ambient temperature than M1.

Figure 5 shows the median 24-h temperature profile of M1, dome air, and outside air for nights in which GPI took on-sky data. It shows that the min-to-max range of M1 is small compared with the min-to-max range of the ambient air. We postulate that M1 typically remains warmer than ambient air during the night, resulting in additional mirror seeing and in GPI AO performance degradation. The exact thermal balance of any observatory is complex. M1 may never be in good equilibrium after sudden jumps in the ambient temperature, which on Cerro Pachon are frequently >4°C in a day. There could also be potential sources of heat such as electronics in or near the mirror cell. This is an ongoing area of study at the Gemini Observatory.

4.2 Effect of Temperature Differentials on Residual Wavefront Error and Contrast

Next we explored the correlation between the instantaneous σ_{WFE} recorded in the GPI image headers and the temperature differences between M1 and the outside air. The result, which is
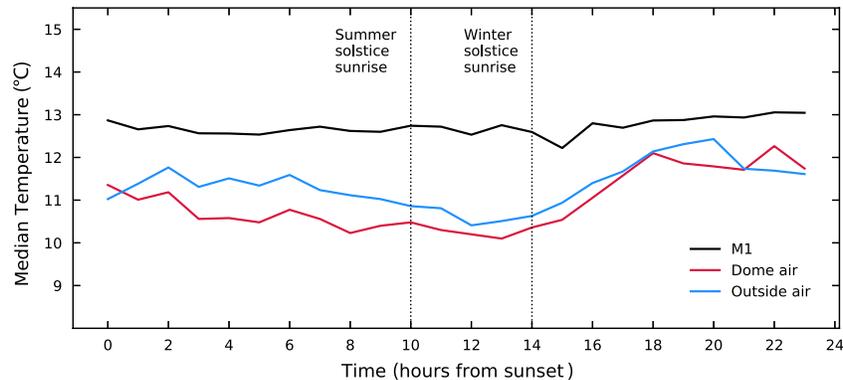

Fig. 5 Median 24-h temperature profile at GS for nights on which GPI took on-sky data. The black, red, and blue lines represent the median temperature of M1, dome air, and the outside air, respectively. Vertical dashed lines mark the approximate length of the shortest and longest nights of the year.
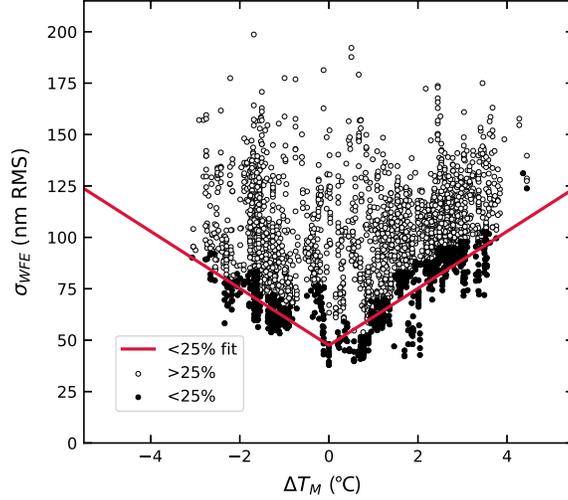
Fig. 6 σ_{WFE} versus ΔT_{M}. The temperature difference between M1 and ambient sets the lower limit on σ_{WFE}. The red line indicates a fit of the bottom 25th percentile of the data, which are the points shaded in black.

displayed in Fig. 6, shows that σ_{WFE} becomes larger as the temperature difference between M1 and the outside air increases. Some vertical scatter is present due to additional contributions from other sources affecting performance, such as stellar magnitude or atmospheric seeing conditions. With appropriate calibration, measurements from the observatory seeing monitors could potentially be used to correct for some of the atmospheric seeing contribution; this analysis is left to future work. Nonetheless, the performance limit imposed by mirror seeing is clearly captured by the lower envelope of the data, which corresponds to the best seeing conditions. The model[43] we used to capture the relationship between σ_{WFE} and ΔT_{M} is

$$\sigma_{\mathrm{WFE}} = a|\Delta T_{\mathrm{M}}| + b, \tag{8}$$

where a and b are free parameters. To isolate the impact of ΔT_{M}, we only fit the bottom 25th percentile of each 0.5°C temperature difference bin. The resulting fit is

$$\sigma_{\mathrm{WFE}} = (13.9 \pm 0.4)|\Delta T_{\mathrm{M}}| + (47.5 \pm 0.7) \ (\mathrm{nm \ RMS}). \tag{9}$$

Our fit predicts that we obtain an additional 41.6 ± 1.2 nm of wavefront error when M1 is 3°C warmer than the outside air. This behavior is consistent with results from previous studies of mirror seeing[25–27] when $\Delta T_{\mathrm{M}} > 0°$C. Past studies observed a weaker effect at $\Delta T_{\mathrm{M}} < 0°$C. Our data are consistent with an equal slope at both warmer and cooler temperatures, although hints of a weaker effect at cooler temperatures are present. We note that our data span a larger range of negative temperatures than most previous studies.

We also quantified the effects of mirror seeing on contrast performance, which is the quantity of interest when imaging planets. Previous correlation studies of GPI performance showed that raw contrast and final contrast both scaled with σ_{WFE}^2 at close-to-intermediate separations.[10,11] Therefore, we expected that raw contrast and final contrast to have the following relationship:

$$\mathrm{Contrast \ at \ 0.4 \ arc \ sec} = c\Delta T_{\mathrm{M}}^2 + d, \tag{10}$$

where c and d are free parameters. Figure 7 displays raw contrast (left) and final contrast (right) plotted as a function of ΔT_{M}. Once again, we see that the temperature difference sets a floor to the achievable contrast. For both raw and final contrast, we again fit only the bottom 25th percentile of each 0.5°C temperature difference bin. The fit for raw contrast is

$$\mathrm{Contrast \ at \ 0.4 \ arc \ sec} = (7.3 \pm 0.1)10^{-6}\Delta \mathrm{T}_{\mathrm{M}}^2 + (3.6 \pm 0.1)10^{-5}, \tag{11}$$
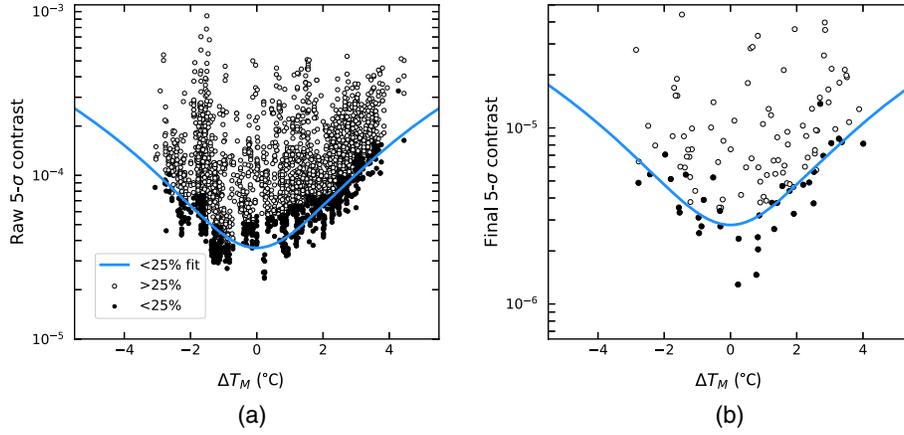
and the fit for final contrast is

Fig. 7 Image contrast versus ΔT_{M}. (a) Raw contrast while (b) is final contrast. Blue line is the fit of the best 25th percentile of the data (black points). On nights when the temperature of the mirror diverged by more than 3°C from the outside air temperature, both raw and final contrast degraded by ~3×.

$$\text{Contrast at } 0.4 \text{ arc sec} = (3.4 \pm 0.6)10^{-7}\Delta T_{\mathrm{M}}^2 + (1.4 \pm 0.3)10^{-6}. \tag{12}$$

Our fits show that when M1 is 3°C warmer than the outside air, both raw and contrast degrade by a factor of 3 ± 1. This is an apparent discrepancy with the Ref. 44 results for the Keck/NIRC2 Vortex Coronagraph instrument performance, which did not find a relationship between achievable contrast and temperature differences. However, an overwhelming majority of their data had $\Delta T_{\mathrm{M}} < 0.5$°C, where we see only a very weak effect. Furthermore, Ref. 44 fit all of their data, not only the best 25th percentile. We believe that these two factors account for the apparent discrepancy.

4.3 *Effect of Temperature Differentials on Turbulence Power Spectra*

Evidently high-contrast imaging performance is reduced significantly when M1 is not in thermal equilibrium; however, this relationship alone cannot identify the underlying cause. As discussed in Sec. 1, GPI's AO system was designed assuming Kolmogorov turbulence models of the local atmosphere. Perhaps M1 is an extra source of turbulence, resulting in turbulence conditions for which the AO system is no longer optimized. The GS seeing monitors, located outside the dome, cannot directly measure mirror turbulence. However, GPI's well-characterized AO system may be able to. In this section, we check for relationships between the structure of the spatial and temporal PSDs and ΔT_{M} measured during the entire GPIES campaign. The spatial PSD is calculated with all temporal frequencies, and we fit only spatial frequencies between 0.3 and 1.0 m^{-1}. The temporal PSD is calculated using all spatial frequencies, and we fit only temporal frequencies between 2 and 40 Hz. Therefore, keep in mind that we cannot rule out effects at other length scales or frequencies. After the data selection outlined in Sec. 3.1, a total of 582 AO telemetry sets remained. We then averaged the parameters that were extracted from the fits for all telemetry sets taken while integrating on the same star, leaving 122 measurements.

The parameters extracted from our fits, $\log(\alpha)$ and (β), are plotted as a function of ΔT_{M} in Fig. 8. We find that there is no clear dependence between β and ΔT_{M}. The β_s data are uniformly scattered on the expected power-law for spatial Kolmogorov turbulence ($-11/3$), indicating that mirror seeing does not exhibit significant deviations from Kolmogorov behavior at these length scales. The β_t data also exhibit uniform behavior, but at a slightly higher value than the expected power-law for temporal Kolmogorov turbulence ($-8/3$). This shows that the temporal power spectrum is flatter than what is expected from Kolmogorov, implying an excess of high temporal frequencies with respect to simply translating a Kolmogorov phase screen. Disentangling the relative contributions of noise versus small-spatial-scale boiling is left to future work.
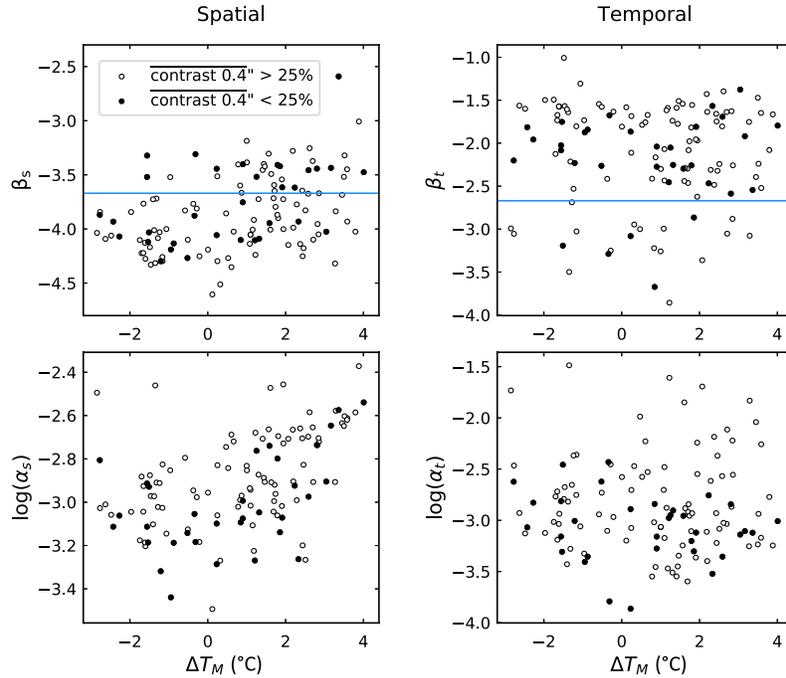
Fig. 8 Power law index (β) and log [amplitude (α)] derived from fits of spatial and temporal PSDs are plotted as a function of ΔT_M. The points are the mean of each campaign sequence. The black points highlight those datasets with the best 25th percentile contrast, as defined in Fig. 7. The power law expected for spatial Kolmogorov turbulence (-3.67) and for temporal Kolmogorov turbulence (-2.67) is marked with a line. Only the strength of the turbulence as measured by the spatial PSD shows clear dependence on ΔT_M.

Now we focus on α, which is directly related to the total seeing.[45] We expect the total seeing to increase as the mirror temperature difference increases, and indeed we find a positive trend between α_s and ΔT_M, albeit at low signal to noise. This, combined with the flat dependence of β_s on ΔT_M, shows that the power spectrum is shifted vertically upward when ΔT_M increases, implying that the intensity of turbulence gets increased at all length scales in the inertial range. Surprisingly, this behavior is less obvious with α_t, but we hypothesize that our inability to probe smaller length scales and/or other noise sources could be obscuring the trend.

5 Conclusion

In this analysis, we studied the effect of the temperature difference (ΔT_M) between the primary mirror (M1) and the outside air, a proxy for mirror seeing, on the performance of the GPI at the GS. Our analysis included 2977 60-s single exposures, 120 fully reduced observing sequences, and 582 AO telemetry sets recorded between September 2014 and February 2017 during the GPIES campaign, as well as contemporaneous temperature and atmospheric seeing measurements. We found that M1 is often warmer than ambient temperature.

We demonstrated that GPI's sensitivity to planets is directly impacted by these temperature differences. Indeed, the best single image (raw) contrast and full sequence (final) contrast performance occurred when ΔT_M was closest to 0°C. The raw and final image contrasts degrade by a factor of 3 ± 1 when $\Delta T_M = 3$°C. We also analyzed the spatial and temporal PSDs derived from AO system telemetry by fitting a power-law to the inertial region of the spectrum (0.3 and 1.0 m^{-1}) and (2 and 40 Hz). We found that mirror seeing increased the intensity of turbulence at all length scales in the inertial range, as evidenced by the increase in the spatial PSD amplitude (α_s) with ΔT_M. We also found that in these frequencies mirror seeing was neither more nor less Kolmogorov than turbulence measured when M1 was in equilibrium with the ambient air. Finally, all datasets showed some deviations from one-layer frozen-flow expectations, the root cause of which is left to future work.

We argue that improvements to the GS dome air and mirror temperature control strategies could improve performance of GPI and other AO instruments. A possible remediation could involve actively cooling M1 during the day with cooling plates behind the glass, which are capable of lowering M1's temperature by 1°C/h.[46] Alternatively, some studies have shown that slowly blowing a stream of cold air above the mirror surface may reduce mirror seeing effects,[26] although this technique has not been tested in high-contrast imaging applications. The observatory staff at GS are continuing to investigate the issue and are in the process of installing a cross-primary laser system that will measure M1 seeing directly.

Our results are generalizable to general-purpose AO systems. The factor of 3 contrast degradation that GPI sees when $\Delta T_{\mathrm{M}} = 3^{\circ}$C roughly corresponds to a factor of $\sqrt{3}$ increase in wavefront error. Telescope temperature control is critical for maximizing the performance of any AO instrument.

References

1. C. Marois et al., "Direct imaging of multiple planets orbiting the star HR 8799," *Science* **322**, 1348–1352 (2008).
2. E. L. Nielsen et al., "The Gemini NICI planet-finding campaign: the orbit of the young exoplanet β Pictoris b," *Astrophys. J.* **794**, 158 (2014).
3. B. Macintosh et al., "Discovery and spectroscopy of the young Jovian planet 51 Eri b with the Gemini Planet Imager," *Science* **350**, 64–67 (2015).
4. B. P. Bowler, "Imaging extrasolar giant planets," *Proc. Astron. Soc. Pac.* **128**, 102001 (2016).
5. A. Rajan et al., "Characterizing 51 Eri b from 1 to 5 μm: a partly cloudy exoplanet," *Astron. J.* **154**, 10 (2017).
6. M. Keppler et al., "Discovery of a planetary-mass companion within the gap of the transition disk around PDS 70," *Astron. Astrophys.* **617**, A44 (2018).
7. J. M. Stone et al., "The LEECH exoplanet imaging survey: limits on planet occurrence rates under conservative assumptions," *Astron. J.* **156**, 286 (2018).
8. R. Soummer et al., "The Gemini Planet Imager coronagraph testbed," *Proc. SPIE* **7440**, 74400R (2009).
9. B. Macintosh et al., "First light of the Gemini Planet Imager," *Proc. Natl. Acad. Sci. U.S.A.* **111**, 12661–12666 (2014).
10. L. A. Poyneer et al., "Performance of the Gemini Planet Imager's adaptive optics system," *Appl. Opt.* **55**, 323–340 (2016).
11. V. P. Bailey et al., "Status and performance of the Gemini Planet Imager adaptive optics system," *Proc. SPIE* **9909**, 99090V (2016).
12. J. Milli et al., "Performance of the extreme-AO instrument VLT/SPHERE and dependence on the atmospheric conditions," in *AO4ELT5 Conf. Ser.*, 10.26698, p. 34 (2017).

13. R. Racine et al., "Speckle noise and the detection of faint companions," *Proc. Astron. Soc. Pac.* **111**, 587–594 (1999).
14. M. D. Perrin et al., "The structure of high Strehl ratio point-spread functions," *Astrophys. J.* **596**, 702–712 (2003).
15. A. Madurowicz et al., "Characterization of lemniscate atmospheric aberrations in Gemini Planet Imager data," *Proc. SPIE* **10703**, 107036E (2018).
16. F. Cantalloube et al., "Origin of the asymmetry of the wind driven halo observed in high-contrast images," *Astron. Astrophys.* **620**, L10 (2018).
17. J. Milli et al., "Low wind effect on VLT/SPHERE: impact, mitigation strategy, and results," *Proc. SPIE* **10703**, 107032A (2018).
18. T. de Karman and L. Howarth, "On the statistical theory of isotropic turbulence," *Proc. R. Soc. London Ser. A* **164**, 192–215 (1938).
19. D. L. Fried, "Limiting resolution looking down through the atmosphere," *J. Opt. Soc. Am.* **56**, 1380–1384 (1966).
20. J. W. Hardy, *Adaptive Optics for Astronomical Telescopes*, Oxford University Press, Oxford (1998).
21. V. I. Tatarskii, *Wave Propagation in Turbulent Medium*, Dover Books on Physics and Mathematical Physics, Dover, New York (1961).
22. F. Roddier, "The effects of atmospheric turbulence in optical astronomy," *Prog. Opt.* **19**, 281–376 (1981).
23. G. I. Taylor, "The spectrum of turbulence," *Proc. R. Soc. London Ser. A* **164**, 476–490 (1938).
24. J. M. Conan, G. Rousset, and P. Y. Madec, "Wave-front temporal spectra in high-resolution imaging through turbulence," *J. Opt. Soc. Am. A* **12**, 1559–1570 (1995).
25. R. Racine et al., "Mirror, dome, and natural seeing at CFHT," *Proc. Astron. Soc. Pac.* **103**, 1020 (1991).
26. C. M. Lowne, "An investigation of the effects of mirror temperature upon telescope seeing," *Mon. Not. R. Astron. Soc.* **188**, 249–259 (1979).
27. M. Iye et al., "Evaluation of seeing on a 62-cm mirror," *Proc. Astron. Soc. Pac.* **103**, 712 (1991).
28. R. Jensen-Clem et al., "The performance of the Robo-AO laser guide star adaptive optics system at the Kitt Peak 2.1 m Telescope," *Astron. J.* **155**, 32 (2018).
29. E. Nielsen et al., "The Gemini Planet Imager Exoplanet Survey: giant planet and brown dwarf demographics from 10 to 100 AU," *Astron. J.* **158**, 13 (2019).
30. M. D. Perrin et al., "Gemini Planet Imager observational calibrations I: overview of the GPI data reduction pipeline," *Proc. SPIE* **9147**, 91473J (2014).
31. J. J. Wang et al., "pyKLIP: PSF subtraction for exoplanets and disks," Astrophysics Source Code Library (2015).
32. M. D. Perrin et al., "Gemini Planet Imager observational calibrations XI: pipeline improvements and enhanced calibrations after two years on sky," *Proc. SPIE* **9908**, 990837 (2016).
33. J.-B. Ruffio et al., "Improving and assessing planet sensitivity of the GPI Exoplanet Survey with a forward model matched filter," *Astrophys. J.* **842**, 14 (2017).
34. J. J. Wang et al., "The automated data processing architecture for the GPI Exoplanet Survey," *Proc. SPIE* **10400**, 1040026 (2017).
35. L. A. Poyneer, D. T. Gavel, and J. M. Brase, "Fast wave-front reconstruction in large adaptive optics systems with use of the Fourier transform," *J. Opt. Soc. Am. A* **19**, 2100–2111 (2002).
36. Minco, "Resistance thermometer, S651PDX24B," https://www.minco.com/products/sense/temperature/surfacesensor (accessed 6 October 2019).
37. Omega, "Air temperature RTD sensors, RTD-805," https://www.omega.com/en-us/sensors-and-sensing-equipment/temperature/sensors/rtd-sensors/p/RTD-805-RTD-806 (accessed 6 October 2019).
38. A. Tokovinin and V. Kornilov, "Accurate seeing measurements with MASS and DIMM," *Mon. Not. R. Astron. Soc.* **381**, 1179–1189 (2007).
39. L. Poyneer, M. van Dam, and J.-P. Véran, "Experimental verification of the frozen flow atmospheric turbulence assumption with use of astronomical adaptive optics telemetry," *J. Opt. Soc. Am. A* **26**, 833 (2009).

40. S. Srinath et al., "Computationally efficient autoregressive method for generating phase screens with frozen flow and turbulence in optical simulations," *Opt. Express* **23**, 33335–33349 (2015).

41. M. Perrin et al., "POPPY: physical optics propagation in PYthon," Astrophysics Source Code Library (2016).

42. A. Savitzky and M. J. E. Golay, "Smoothing and differentiation of data by simplified least squares procedures," *Anal. Chem.* **36**, 1627–1639 (1964).

43. M. Tallis et al., "Air, telescope, and instrument temperature effects on the Gemini Planet Imager's image quality," *Proc. SPIE* **10703**, 1070356 (2018).

44. W. J. Xuan et al., "Characterizing the performance of the NIRC2 vortex coronagraph at W. M. Keck Observatory," *Astron. J.* **156**, 156 (2018).

45. R. J. L. Fétick et al., "Physics-based model of the adaptive-optics-corrected point spread function—applications to the SPHERE/ZIMPOL and MUSE instruments," *Astron. Astrophys.* **628**, A99 (2019).

46. R. J. S. Greenhalgh, L. M. Stepp, and E. R. Hansen, "Gemini primary mirror thermal management system," *Proc. SPIE* **2199**, 911–921 (1994).

Biographies of the authors are not available.